

On the violation of the zeroth law of turbulence in space plasmas

R. Meyrand¹, †, J. Squire¹, A. A. Schekochihin^{2,3}, and W. Dorland⁴

¹Department of Physics, University of Otago, 730 Cumberland St., Dunedin 9016, New Zealand

²The Rudolf Peierls Centre for Theoretical Physics, University of Oxford, Clarendon Laboratory, Parks Road, Oxford, OX1 3PU, UK

³Merton College, Merton Street, Oxford OX1 4JD, UK

⁴Department of Physics, University of Maryland, College Park, MD 20742, USA

(Received xx; revised xx; accepted xx)

The zeroth law of turbulence states that, for fixed energy input into large-scale motions, the statistical steady state of a turbulent system is independent of microphysical dissipation properties. This behavior, which is fundamental to nearly all fluid-like systems from industrial processes to galaxies, occurs because nonlinear processes generate smaller and smaller scales in the flow, until the dissipation—no matter how small—can thermalise the energy input. Using direct numerical simulations and theoretical arguments, we show that in strongly magnetised plasma turbulence such as that recently observed by the Parker Solar Probe (PSP) spacecraft, the zeroth law is routinely violated. Namely, when such turbulence is “imbalanced”—when the large-scale energy input is dominated by Alfvénic perturbations propagating in one direction (the most common situation in space plasmas)—nonlinear conservation laws imply the existence of a “barrier” at scales near the ion gyroradius. This causes energy to build up over time at large scales. The resulting magnetic-energy spectra bear a strong resemblance to those observed in situ, exhibiting a sharp, steep kinetic transition range above and around the ion-Larmor scale, with flattening at yet smaller scales. The effect thus offers a possible solution to the decade-long puzzle of the position and variability of ion-kinetic spectral breaks in plasma turbulence. The existence of the “barrier” also suggests that how a plasma is forced at large scales (the imbalance) may have a crucial influence on thermodynamic properties such as the ion-to-electron heating ratio.

1. Introduction

In his celebrated 1850 manuscript “The Mechanical Equivalent of Heat” (Joule 1850), James Prescott Joule described how a liquid stirred by a falling mass would heat up by a well-defined, fixed amount, thus demonstrating the equivalence of mechanical work and heat. Though less well appreciated, Joule’s study also revealed another, similarly intriguing law of nature: his series of experiments, which measured the work done by different masses on either water or mercury at high ($\gtrsim 10^5$) Reynolds number, showed that the damping rate of the liquid’s kinetic energy must be proportional to its velocity, rather than its viscosity. This is despite the fact that it is the viscosity that is ultimately responsible for the conversion of work to heat. The general principle, which has subsequently become known as the “zeroth law of turbulence,” states that the dissipation rate of a high-Reynolds-number turbulent flow under fixed large-scale conditions is

† Email address for correspondence: romain.meyrand@otago.ac.nz

independent of the value or mechanism of the microphysical energy dissipation (e.g., the viscosity). This distinctive property arises because turbulence nonlinearly generates motions at successively smaller scales, always reaching the scale where viscous effects become large, no matter how small the viscosity itself.

Collisionless plasmas, although far more complex than water and mercury as used in Joule’s experiments, are generally assumed to satisfy the zeroth law. Energy injected into smooth, large-scale fluctuations in position and velocity space (phase space)—for example, Alfvénic perturbations emitted from the Sun’s corona—must make its way (linearly or nonlinearly) towards small scales before it can be converted to heat. If this is not possible—if the zeroth law is violated—the injected energy will not be efficiently thermalised, instead building up over time in large-scale motions and magnetic fields. An inability of the system to transfer energy to small scales thus has a dramatic impact on the large-scale behavior of the plasma. In this paper, we argue that, counter to the assumptions of much previous work, the zeroth law can be violated strongly in magnetised (Alfvénic) plasma turbulence such as that observed in the solar wind. The effect, which occurs when the turbulence is “imbalanced” (i.e., when the energies of forward and backward propagating fluctuations differ), arises because both energy and a “generalised helicity” (see Eq. (2.9)) are nonlinearly conserved in strongly magnetised (low-beta) collisionless plasmas. At scales above the ion gyroradius ρ_i , the generalised helicity is the magnetohydrodynamic (MHD) cross-helicity and naturally undergoes a forward cascade (nonlinear energy transfer to small scales); at scales below ρ_i , the generalised helicity becomes magnetic helicity and naturally undergoes an inverse cascade (nonlinear transfer to larger scales; Cho 2011). The collision of the two cascades creates a “helicity barrier”: it stops the system from dissipating injected energy through nonlinear transfer to smaller spatial scales.

The resulting turbulence, which we illustrate in Figs. 1 and 2, bears a strong resemblance to recent measurements from the Parker Solar Probe (PSP) spacecraft and others. While balanced turbulence shows the expected transition from Alfvénic to kinetic-Alfvén-wave (KAW) turbulence at ρ_i scales (Howes *et al.* 2008; Schekochihin *et al.* 2009), in imbalanced turbulence (purple lines in Fig. 2), the ion-kinetic transition, which is instead controlled by the helicity barrier, is both much sharper and occurs at a larger scale. The break in the spectrum is dramatic, with a very steep spectral slope in the transition range, causing manifest differences in the turbulent flow structure compared to balanced turbulence (Fig. 1). Despite the cascade barrier, the energy exhibits a standard $\sim k^{-3/2}$ spectrum (Boldyrev 2006) above the transition.[†] At yet smaller scales, a spectral flattening (approaching the $\sim k^{-2.8}$ spectrum expected for KAW turbulence; Schekochihin *et al.* 2009; Alexandrova *et al.* 2009, 2012; Boldyrev *et al.* 2013) is observed due to small leakage through the barrier (see § 3.2). The behavior matches observations of near-Sun imbalanced turbulence from PSP, which often show clear spectral breaks significantly above the ion-Larmor scale, with a nonuniversal spectrum between the break and a flatter spectrum at yet smaller scales (Bowen *et al.* 2020a; Duan *et al.* 2021). In our theory, which differs from previous phenomenologies that assume either an enhanced cascade rate or energy dissipation around ρ_i scales (e.g., Voitenko & De Keyser 2016; Mallet *et al.* 2017), the spectral break occurs around the scale at which the helicity barrier

[†] The range in which it is observed here is not wide enough to distinguish between $k^{-3/2}$ (Maron & Goldreich 2001; Boldyrev 2006; Perez *et al.* 2012) and $k^{-5/3}$ (Goldreich & Sridhar 1995; Beresnyak 2014), but this RMHD-range scaling is not the point of this work. We will compare to $k^{-3/2}$ where necessary because it is well motivated in balanced turbulence and supported by observations (Chen *et al.* 2020).

halts the energy flux, and this barrier moves to larger scales as the outer-scale energy grows with time. Final saturation, which occurs only after many Alfvén crossing times and depends on simulation resolution, relies on fluctuations reaching large amplitudes and dissipating through nonuniversal (and, in our simulations, artificial) means. This suggests that observed turbulent cascades in the solar wind may not be in a saturated state where energy input balances dissipation. It may also explain the observed non-universality of the break scale and of the sub-break spectral scaling.

The remainder of the paper is organised as follows. Section 2 provides the theoretical framework our study, starting with the minimal “Finite-Larmor-Radius MHD” model (§ 2.1) used for theoretical arguments and simulations throughout this work. This is followed by a brief overview of imbalanced turbulence (§ 2.2) before the presentation of our main theoretical result – a simple proof that energy and generalised helicity cannot both cascade to arbitrarily small (sub- ρ_i) perpendicular scales, thus causing violation of the zeroth law (§ 2.3). Numerical results, including the details of the methods used to produce Figs. 1 and 2, are covered in § 3. We start with numerical demonstrations of the zeroth-law violation in both the perpendicular and parallel directions (Fig. 3), before considering in more detail the properties of turbulence that is affected by the helicity barrier (§§ 3.2.1 and 3.2.2). Finally, we explore the possible consequences of our results for space plasmas in § 4. We consider the potential impact of other plasma effects that are not contained in our model, followed by a qualitative discussion of how our predictions compare to in-situ observations of solar-wind turbulence (§ 4.2).

2. Theoretical Framework

Before continuing, we define the following symbols, with α signifying species (either ions, $\alpha = i$, or electrons, $\alpha = e$): $n_{0\alpha}$ is the background density; $T_{0\alpha}$ is the background temperature and $\tau = T_{0i}/T_{0e}$; \mathbf{B} is the magnetic field, with $\mathbf{B}_0 = B_0\hat{\mathbf{z}}$ the background; $\beta_\alpha = 8\pi n_{0\alpha}T_{0\alpha}/B_0^2$ is the ratio of thermal to magnetic energy; m_α is the particle mass; q_α is the particle charge with $q_e = -e$ and $q_i = Ze$; $\Omega_\alpha = |q_\alpha|B_0/m_\alpha c$ is the gyroradius; $\rho_\alpha = c\sqrt{2m_\alpha T_{0\alpha}}/|q_\alpha|B_0$ is the gyroradius; $d_\alpha = \rho_\alpha/\sqrt{\beta_\alpha}$ is the skin depth; c is the speed of light; and $v_A = B_0/\sqrt{4\pi n_{0i}m_i}$ is the Alfvén speed.

In order to elucidate the key physical processes involved in this highly complex problem, our approach is to use the simplest plasma model that meets two important requirements: (i) it can be formally (asymptotically) derived in a physically relevant limit, which allows us to evaluate critically the plasma regimes in which our results remain valid; and (ii) it remains valid for perpendicular scales both above and below the ρ_i scale, which is clearly a necessity for a study of the ion-kinetic transition. The minimal model of *Finite-Larmor-Radius MHD* (FLR-MHD) described below meets these requirements (Passot *et al.* 2018; Schekochihin *et al.* 2019), while avoiding the serious complexity of solving kinetic equations in phase space. It is formally valid for low-frequency Alfvénic fluctuations in a $\beta_e \ll 1$ plasma, at perpendicular scales above d_e and ρ_e . Because $\rho_e \ll d_e$ at $\beta_e \ll 1$ and $d_e/\rho_i = (m_e/m_i)^{1/2}/\sqrt{\beta_i}$ in a neutral plasma, so long as $\beta_i > m_e/m_i$ and $\beta_i \sim \beta_e$, FLR-MHD provides a valid description of the ion-kinetic transition. The low- β assumption is well satisfied in many astrophysical and space plasmas, including in the solar corona and the near-Sun solar wind (Bruno & Carbone 2013).

2.1. FLR-MHD Model

FLR-MHD can be self-consistently derived from the Vlasov equation, starting with the assumptions that all fields (the magnetic field, flow velocity etc.) vary slowly in time compared to the ion-cyclotron frequency, that there is a strong background magnetic

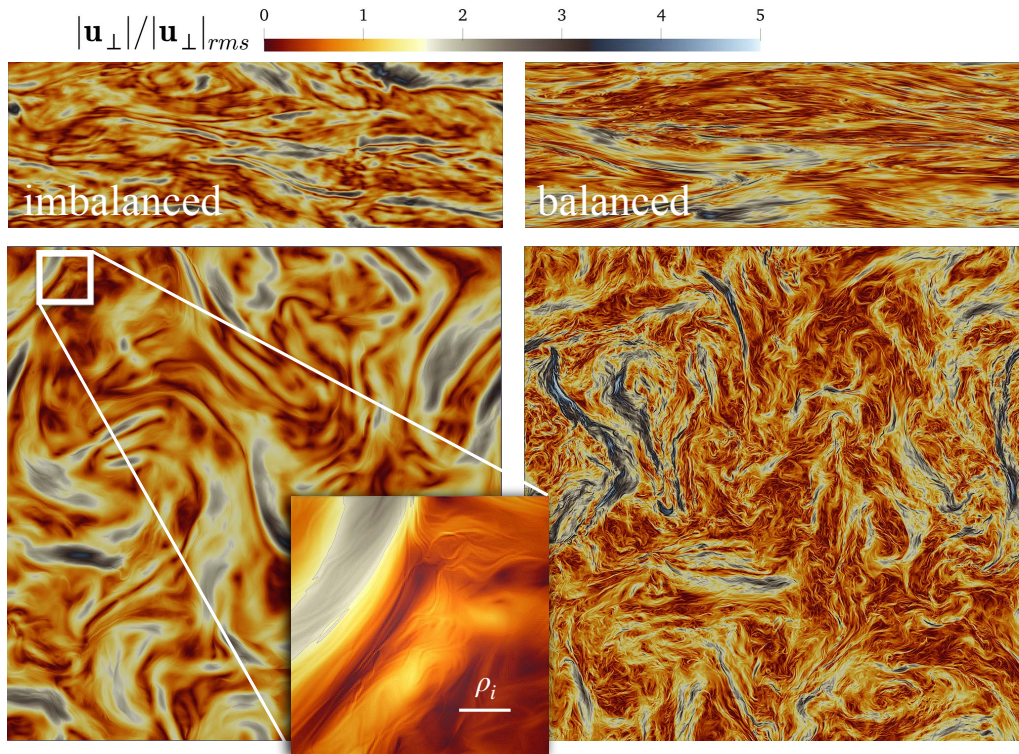


FIGURE 1. The spatial structure of the perpendicular electron flow \mathbf{u}_\perp , or equivalently, the perpendicular electric field $\mathbf{E}_\perp = -\nabla_\perp \varphi$ [see Eqs. (2.2) to (2.3)]. We compare imbalanced and balanced turbulence in the left and right panels, respectively. Top panels show a parallel (x, z) slice ($\mathbf{B}_0 = B_0 \hat{z}$ left to right), bottom panels show a perpendicular (x, y) slice (\mathbf{B}_0 out of the page). The dramatic dependence on imbalance arises because imbalanced turbulence is afflicted by the “helicity barrier”: at a nonuniversal scale $k_\perp^* \rho_i \lesssim 1$ most of the energy cascade of the dominant component (E^+) cannot proceed to smaller scales, violating the zeroth law of turbulence. The resulting sharp break in the spectrum is shown in Fig. 2, and is followed by the re-emergence of a cascade at yet smaller scales (see zoomed region of left-hand panel). These simulations have a resolution of 2048^3 and are initialised by refining the 256^3 simulations of Figs. 4–6, starting at $t \approx 18\tau_A$.

field, and that the correlation length l_\parallel of a perturbation in the field-parallel direction is much larger than its field-perpendicular correlation length l_\perp (Schekochihin *et al.* 2009). The resulting system (gyrokinetics) is still quite complex, and significant further simplification is possible using an expansion in $\beta_e \sim \beta_i \ll 1$ (Zocco & Schekochihin 2011; Schekochihin *et al.* 2019). In this case, the ion-thermal speed is small compared to the Alfvén speed, implying there is minimal coupling between perpendicular (Alfvénic) motions and ion-compressive (kinetic) degrees of freedom, even for ion-Larmor-scale fluctuations (Schekochihin *et al.* 2019). This means that energy injected into Alfvénic motions at the largest scales ($l_\perp \gg \rho_i$) cannot directly heat ions (within the low-frequency approximation), allowing the formulation of a simple closed set of fluid equations (i.e., equations in 3-D space) to describe the Alfvénic component of the turbulence both above and below the ρ_i scale.[†] These are the FLR-MHD equations. We note that the assumption

[†] Compressive fluctuations, which cascade passively to ρ_i scales, where they likely heat the ions through nonlinear phase mixing (Meyrand *et al.* 2019; Kawazura *et al.* 2020), can modify the equations around ρ_i scales by changing the relationship between δn_e and φ (although they

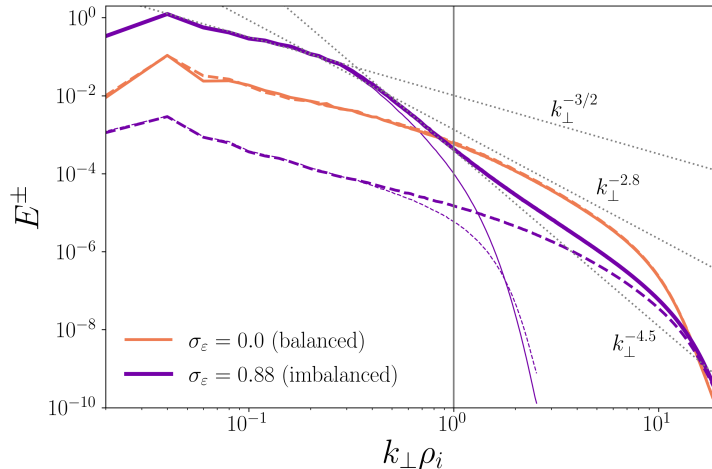


FIGURE 2. Energy spectra for the simulations pictured in Fig. 1. Purple and orange lines show imbalanced and balanced turbulence, respectively, while solid and dashed lines show the dominant (E^+) and subdominant (E^-) energies, respectively [see Eq. (2.7)]. Thin lines show the spectra of the 256^3 imbalanced simulation at the same time and parameters (see Fig. 5), emphasising the re-emergence of a kinetic-Alfvén-wave cascade ($\sim k_\perp^{-2.8}$) at small scales in imbalanced turbulence, if a sufficient range of scales is available. The resulting double-kinked spectrum strongly resembles those observed in the solar wind (Sahraoui *et al.* 2009; Bowen *et al.* 2020a). As far as we know, this is the first time such spectra have been reproduced in a numerical simulation.

$l_\perp \ll l_\parallel$, which is well tested in the solar wind (Chen 2016), is satisfied in standard magnetised plasma turbulence phenomenologies (Goldreich & Sridhar 1995; Boldyrev 2006; Schekochihin 2020). The key idea is that of a “critical balance” between linear and nonlinear times at all scales, which leads to the estimate $l_\parallel \sim l_\perp^{1/2} \gg l_\perp$ (Boldyrev 2006; Mallet & Schekochihin 2017). At electron-skin-depth scales ($l_\perp \sim d_e$) where the magnetic field is no longer frozen into the electron flow, FLR-MHD breaks down due to coupling to the electron distribution function. Although a model exists to capture this transition accurately (Zocco & Schekochihin 2011), its additional complexity is unnecessary for describing the ion-kinetic transition of interest here. We thus focus on scales above d_e , which also implies $\beta_i > m_e/m_i$ so that $d_e < \rho_i$.

The FLR-MHD equations are

$$\left(\frac{\partial}{\partial t} + \mathbf{u}_\perp \cdot \nabla_\perp \right) \frac{\delta n_e}{n_{0e}} = -\frac{c}{4\pi e n_{0e}} \left(\frac{\partial}{\partial z} + \mathbf{b}_\perp \cdot \nabla_\perp \right) \nabla_\perp^2 A_\parallel + \mathcal{D}_{6\nu} \frac{\delta n_e}{n_{0e}}, \quad (2.1)$$

$$\left(\frac{\partial}{\partial t} + \mathbf{u}_\perp \cdot \nabla_\perp \right) A_\parallel = -c \frac{\partial \varphi}{\partial z} + \frac{c T_{0e}}{e} \left(\frac{\partial}{\partial z} + \mathbf{b}_\perp \cdot \nabla_\perp \right) \frac{\delta n_e}{n_{0e}} + \mathcal{D}_{6\nu} A_\parallel, \quad (2.2)$$

$$\frac{\delta n_e}{n_{0e}} = -\frac{Z}{\tau} \left(1 - \hat{T}_0 \right) \frac{e\varphi}{T_{0e}}, \quad (2.3)$$

where $\delta n_e/n_{0e} = \delta n_i/n_{0i}$ is the perturbed electron (and, by quasi-neutrality, ion) density, A_\parallel is the $\hat{\mathbf{z}}$ component of the vector potential, φ is the electrostatic potential, $\mathbf{u}_\perp = c B_0^{-1} \hat{\mathbf{z}} \times \nabla_\perp \varphi$ is the perpendicular $\mathbf{E} \times \mathbf{B}$ (electron) flow, and $\mathbf{b}_\perp = -B_0^{-1} \hat{\mathbf{z}} \times \nabla_\perp A_\parallel$ is the perturbation of the magnetic field’s direction. The gyrokinetic Poisson operator

cannot exchange energy with Alfvénic fluctuations; Schekochihin *et al.* 2019). We are effectively assuming throughout this work that the energy in the Alfvénic cascade dominates over that in a compressive cascade, which is (mostly) well justified in the solar wind (Chen 2016).

$1 - \hat{I}_0 = 1 - I_0(\alpha)e^{-\alpha}$, with $\alpha = -\rho_i^2 \nabla_\perp^2 / 2$ and I_0 the modified Bessel function, becomes $1 - \hat{I}_0 \approx -\rho_i^2 \nabla_\perp^2 / 2$ for fluctuations with $k_\perp \rho_i \ll 1$, and $1 - \hat{I}_0 \approx 1$ for fluctuations with $k_\perp \rho_i \gg 1$. In the former limit, the FLR-MHD system becomes the well-known Reduced MHD (RMHD) model (Strauss 1976), in the latter it becomes the Electron RMHD model (Schekochihin *et al.* 2009; Boldyrev *et al.* 2013). The hyper-diffusion operator, $\mathcal{D}_{6\nu} = \nu_{6\perp} \nabla_\perp^6 + \nu_{6z} \nabla_z^6$, is necessary in order to dissipate energy above the grid scale in our numerical simulations, but is not intended to model a specific physical process.

2.2. Imbalanced Alfvénic Turbulence

A linearization of Eqs. (2.1)–(2.3), assuming a sinusoidal spatial dependence with wavenumber $\mathbf{k} = k_\perp \hat{\mathbf{x}} + k_z \hat{\mathbf{z}}$, yields forward and backward propagating modes of frequency $\omega = \pm k_z v_{\text{ph}}(k_\perp) v_A$, where

$$v_{\text{ph}}(k_\perp) = \frac{k_\perp \rho_i}{\sqrt{2}} \left(\frac{1}{1 - \hat{I}_0} + \frac{Z}{\tau} \right)^{1/2} \approx \begin{cases} 1 & k_\perp \rho_i \ll 1, \\ \left(\frac{1}{2} + \frac{Z}{2\tau} \right)^{1/2} & k_\perp \rho_i \gg 1. \end{cases} \quad (2.4)$$

FLR-MHD thus recovers shear-Alfvén waves when $k_\perp \rho_i \ll 1$ and (low- β) kinetic Alfvén waves (KAWs) when $k_\perp \rho_i \gg 1$. The eigenfunctions of these linear modes, known as the generalised Elsässer potentials, will provide a useful basis for intuitive discussion of the nonlinear problem and turbulence. At wavenumber \mathbf{k} , these are

$$\Theta_{\mathbf{k}}^\pm = -\Omega_i \frac{v_{\text{ph}}(k_\perp)}{k_\perp^2} \frac{\delta n_e}{n_{0e}} \mp \frac{A_\parallel}{\sqrt{4\pi m_i n_{0i}}}. \quad (2.5)$$

At large scales $k_\perp \rho_i \ll 1$, they have the property $\hat{\mathbf{z}} \times \nabla_\perp \Theta^\pm = \mathbf{Z}^\pm = \mathbf{u}_\perp \pm \mathbf{B}_\perp / \sqrt{4\pi m_i n_{0i}}$, where \mathbf{Z}^\pm are the Elsässer variables (Elsässer 1950).

The utility of Θ^\pm arises from the fact that at large scales (i.e., in the RMHD limit), nonlinear interaction—and thus the turbulent cascade—requires the interaction between \mathbf{Z}^+ and \mathbf{Z}^- (equivalently, Θ^+ and Θ^-). Thus, the difference in amplitude of \mathbf{Z}^+ and \mathbf{Z}^- , which is known as the *energy imbalance* and is determined by the outer-scale forcing of the plasma, has a strong influence on the properties of the turbulent cascade. We will quantify it in the standard way with

$$\sigma_c = \frac{\int d^3 \mathbf{x} (|\mathbf{Z}^+|^2 - |\mathbf{Z}^-|^2)}{\int d^3 \mathbf{x} (|\mathbf{Z}^+|^2 + |\mathbf{Z}^-|^2)}, \quad (2.6)$$

so $\sigma_c = \pm 1$ if $\mathbf{Z}^- = 0$ or $\mathbf{Z}^+ = 0$. Although imbalanced RMHD turbulence remains poorly understood (Perez & Boldyrev 2009; Chandran 2008; Beresnyak & Lazarian 2009; Lithwick *et al.* 2007; Chandran & Perez 2019; Schekochihin 2020), observations show that solar-wind turbulence is usually imbalanced, particularly in near-Sun regions where $|\sigma_c| \gtrsim 0.9$ (McManus *et al.* 2020). This occurs because Alfvénic perturbations are launched outwards from the corona and only generate an inwards propagating component due to their interaction with background density and field gradients (Velli 1993; Chandran & Perez 2019). Our understanding of plasma turbulence thus remains incomplete without addressing the effect of the imbalance on the flow of energy.

At sub-ion scales ($k_\perp \rho_i \gg 1$), the dispersive nature of KAWs makes possible nonlinear interactions between co-propagating perturbations (e.g., Θ^+ with Θ^+). This implies that the two components can exchange energy and that a turbulent cascade is, in principle, possible with just one component Θ^\pm (Cho 2011; Kim & Cho 2015; Voitenko & De Keyser 2016).

2.3. The “Helicity Barrier”

Here we argue that the conservation properties of FLR-MHD imply that a turbulent flux of energy cannot proceed in the usual way to small scales (where it needs to get to be dissipated), violating the zeroth law. We term the barrier in the cascade at scales $l_{\perp} \sim \rho_i$, the “helicity barrier.”

As discussed above, a necessary (though not sufficient) condition for a turbulent system to satisfy the zeroth law is that it has the ability to transfer energy from the largest scales, where energy is assumed to be injected by external processes, to the smallest, where it can be dissipated. The concept can be formalised by the idea of a turbulent “flux” through scale space; if a system is to remain in statistical steady state, each of its nonlinearly conserved invariants with a source at large scales must have an associated flux.[†] This flux must be constant across all scales until the invariant can be dissipated. Importantly, this must hold for *all* nonlinear invariants together: if the flux of one invariant is non-constant and/or insufficient to allow its dissipation, the invariant will change in time, implying that the system is not in steady state. This concept is familiar in the study of two-dimensional hydrodynamics, where the dual conservation of energy and enstrophy stops the flux of energy to small scales, causing both energy and enstrophy to build up in time (in the absence of a large-scale dissipation mechanism). The zeroth law can thus be studied in terms of either the dissipation properties, considering how the dissipation rate varies with microphysical dissipation at fixed large-scale conditions (e.g., [Pearson et al. 2004](#)), or in terms of the large-scale properties, considering how the statistics of the largest scales depend on the microphysical dissipation when the rate of energy injection is fixed. In the following, we examine the conservation laws of FLR-MHD and prove that they do not admit a solution with a constant flux of energy to small perpendicular scales when the energy injection is imbalanced at large scales. This implies that large-scale flows and fields cannot reach steady state through perpendicular dissipation, violating the zeroth law.[‡]

2.3.1. Conservation laws of FLR-MHD

The FLR-MHD system has two nonlinearly conserved quadratic invariants, (free) energy and (generalised) helicity. These are most easily and clearly written in terms of the generalised Elsässer variables. The free energy is

$$E = \frac{1}{4} \sum_{\mathbf{k}} (|k_{\perp} \Theta_{\mathbf{k}}^+|^2 + |k_{\perp} \Theta_{\mathbf{k}}^-|^2), \quad (2.7)$$

[†] The case of decaying turbulence can be more subtle; it clearly violates the zeroth law for some initial conditions, even in hydrodynamics or RMHD. Specifically, if the system decays into a large-scale nonlinear solution – for example, initially imbalanced RMHD turbulence decays into an Elsässer state (only one of \mathbf{Z}^{\pm} , with no nonlinear interactions; see [Dobrowolny et al. 1980](#); [Oughton et al. 1994](#); [Maron & Goldreich 2001](#); [Chen et al. 2011](#)) – the subsequent (slow) decay of this state will clearly depend on the microphysical dissipation.

[‡] The zeroth law is well known to require relatively large Reynolds numbers to be satisfied ([Pearson et al. 2004](#)); indeed, some theories of imbalanced RMHD turbulence ([Chandran 2008](#); [Schekochihin 2020](#)) imply a logarithmic dependence of spectral slopes on dissipation parameters, technically violating the zeroth law. Numerical simulations have yet to yield a definitive verdict on the validity of such theories ([Beresnyak & Lazarian 2009](#); [Schekochihin 2020](#)). The FLR-MHD results below, however, demonstrate a far more brutal zeroth-law violation than these RMHD theories, because they imply that the system’s conserved invariants cannot dissipate. Accordingly, our focus here is not on subtle details of Reynolds-number dependence or whether RMHD can also (modestly) violate the zeroth law. In any case, our simulations provide direct comparisons of FLR-MHD to RMHD, showing that they differ markedly in their large-scale saturation properties.

which reduces to

$$E \approx \frac{1}{4} \int \frac{d^3 \mathbf{x}}{V} (|\mathbf{Z}^+|^2 + |\mathbf{Z}^-|^2) = \frac{1}{2} \int \frac{d^3 \mathbf{x}}{V} \left(|\mathbf{u}_\perp|^2 + \frac{|\mathbf{B}_\perp|^2}{4\pi n_{0i} m_i} \right) \quad (2.8)$$

at large scales. The generalised helicity is

$$\mathcal{H} = \frac{1}{4} \sum_{\mathbf{k}} \frac{|k_\perp \Theta_{\mathbf{k}}^+|^2 - |k_\perp \Theta_{\mathbf{k}}^-|^2}{v_{\text{ph}}(k_\perp)}, \quad (2.9)$$

which reduces to the MHD cross-helicity at $k_\perp \rho_i \ll 1$, $\mathcal{H} \propto \int d^3 \mathbf{x} \mathbf{u}_\perp \cdot \mathbf{B}_\perp$, and becomes magnetic helicity at $k_\perp \rho_i \gg 1$, $\mathcal{H} \propto \int d^3 \mathbf{x} \delta B_\parallel A_\parallel$ [†]. If the $k_\perp \rho_i \ll 1$ motions dominate over the smaller scales, the energy imbalance is $\sigma_c \approx \mathcal{H}/E$. We also define the Θ^\pm “energies,” $E^\pm = \sum_{\mathbf{k}} |k_\perp \Theta_{\mathbf{k}}^\pm|^2/4$, along with perpendicular spectra for E , \mathcal{H} , and E^\pm , denoted $E(k_\perp)$, $E_{\mathcal{H}}(k_\perp)$, and $E^\pm(k_\perp)$, respectively.

2.3.2. The inevitability of the helicity barrier

Consider the case where energy and helicity are injected at large scales at the rates ε and $\varepsilon_{\mathcal{H}}$, respectively, with *injection imbalance* $\sigma_\varepsilon \equiv |\varepsilon_{\mathcal{H}}|/\varepsilon$. The conservation laws above tell us that in a statistical steady state, there must be a nonzero energy flux $\Pi(k_\perp)$ and helicity flux $\Pi_{\mathcal{H}}(k_\perp)$ to small scales where they can be dissipated. If we further assume that (i) energy transfer due to nonlinearity is significant only for modes with similar scales (locality), and (ii) parallel dissipation is small because eddies are highly elongated along the magnetic field, then $\Pi(k_\perp)$ and $\Pi_{\mathcal{H}}(k_\perp)$ must be constant between the forcing and dissipation scales. In the following argument, based on [Alexakis & Biferale \(2018\)](#), we assume such a constant-flux solution and find a contradiction, suggesting that this type of solution is not possible in FLR-MHD when $\sigma_\varepsilon \neq 0$. Fundamentally, the contradiction arises because at large scales \mathcal{H} is the RMHD cross-helicity, which undergoes a forward cascade, while at small scales \mathcal{H} is magnetic helicity, which undergoes an inverse cascade ([Schekochihin et al. 2009](#); [Cho 2011](#); [Kim & Cho 2015](#); [Miloshevich et al. 2020](#); [Pouquet et al. 2020](#)).

Mathematically, the constant-flux solution is

$$\Pi(k_\perp) \simeq \varepsilon \simeq \varepsilon_\perp^{\text{diss}} = \nu_n \sum_{k_\perp} k_\perp^{2n} E(k_\perp), \quad (2.10a)$$

$$\Pi_{\mathcal{H}}(k_\perp) \simeq \varepsilon_{\mathcal{H}} \simeq \varepsilon_{\mathcal{H},\perp}^{\text{diss}} = \nu_n \sum_{k_\perp} k_\perp^{2n} E_{\mathcal{H}}(k_\perp), \quad (2.10b)$$

where $\varepsilon_\perp^{\text{diss}}$ and $\varepsilon_{\mathcal{H},\perp}^{\text{diss}}$ are the energy and helicity dissipation rates (we assume hyper-viscous dissipation of δn_e and A_\parallel of the form $\nu_n k_\perp^{2n}$). This solution satisfies the following inequalities:

$$\begin{aligned} |\Pi_{\mathcal{H}}(k_\perp)| &\simeq \nu_n \left| \sum_{p_\perp=k_\perp}^\infty p_\perp^{2n} E_{\mathcal{H}}(p_\perp) \right| \leq \nu_n v_{\text{ph}}^{-1}(k_\perp) \left| \sum_{p_\perp=k_\perp}^\infty p_\perp^{2n} v_{\text{ph}}(p_\perp) E_{\mathcal{H}}(p_\perp) \right| \\ &\leq v_{\text{ph}}^{-1}(k_\perp) \nu_n \sum_{p_\perp=k_\perp}^\infty p_\perp^{2n} E(p_\perp) \simeq v_{\text{ph}}^{-1}(k_\perp) \Pi(k_\perp), \end{aligned} \quad (2.11)$$

where we have used the fact that $v_{\text{ph}}(k_\perp)$ is a monotonically increasing function of k_\perp , as well as the inequality $v_{\text{ph}}(k_\perp) |E_{\mathcal{H}}(k_\perp)| \leq E(k_\perp)$ from Eqs. (2.7)–(2.9). The ratio of fluxes

[†] Here δB_\parallel is the magnetic-field strength perturbation; $\delta B_\parallel \propto \delta n_e$ for $k_\perp \rho_i \gg 1$ ([Schekochihin et al. 2009](#)).

$|\Pi_{\mathcal{H}}(k_{\perp})|/\Pi(k_{\perp}) \simeq \sigma_{\varepsilon}$ must thus satisfy $\sigma_{\varepsilon} \leq 1/v_{\text{ph}}(k_{\perp})$ for all k_{\perp} above the dissipation scales. But $1/v_{\text{ph}}(k_{\perp})$ decreases with k_{\perp} to arbitrarily small values ($v_{\text{ph}} \propto k_{\perp}$ at $k_{\perp}\rho_i \gg 1$). This suggests that, no matter what the injection imbalance, a cascade that tries to proceed to small scales will at some k_{\perp} violate the inequality (2.11)[‡]. In such a case, the constant-flux solution fails, indicating that the system is unable to thermalise energy and helicity input through small-scale dissipation. We further see that the failure occurs only below the scale where $1/v_{\text{ph}}(k_{\perp}) \simeq \sigma_{\varepsilon}$; this is around $k_{\perp}\rho_i \simeq 1$ for $\sigma_{\varepsilon} \approx 0.7$ but moves to larger scales with increasing σ_{ε} . This highlights an interesting difference compared to the well-known inverse energy cascade of two-dimensional hydrodynamics (Fjørtoft 1953; Alexakis & Biferale 2018): while standard inverse cascades inhibit forward transfer already at the injection scale, helicity must first travel to microphysical (ρ_i) scales before it hits the barrier. As a consequence, despite FLR effects not influencing directly the nonlinear interactions at MHD scales, they could strongly influence turbulence statistics at those scales by insulating them from the dissipation scales.

3. Numerical Experiments

The argument above suggests that it is not possible to have a constant flux of both energy and helicity through the ion-kinetic transition scale. It does not, however, elucidate how the system behaves in the presence of continuous imbalanced injection of energy at large scales. For this, we turn to numerical simulations.

3.1. Numerical setup

We solve Eqs. (2.1)–(2.3) using a modified version of the pseudospectral code TURBO (Teaca *et al.* 2009) in a cubic box $L_{\perp} = L_z = L$ with $N_{\perp}^2 \times N_z$ Fourier modes. A third-order modified Williamson (1980) algorithm is used for time stepping. The values of hyper-dissipation coefficients $\nu_{6\perp}$ and ν_{6z} are chosen based on the numerical resolution, ensuring that the energy spectrum falls off sufficiently rapidly before the resolution cutoff. Fluctuations are stirred at large scales by added forcing terms (f^{n_e} and $f^{A_{\parallel}}$) in Eqs. (2.1)–(2.2). This forcing is confined to $0 < k_{\perp} \leq 4\pi/L$ and $|k_z| = 2\pi/L$ and takes the form of negative damping (f^{n_e} and $f^{A_{\parallel}}$ proportional to the large-scale modes of n_e and A_{\parallel}); this method allows the level of energy and helicity injection (ε and $\varepsilon_{\mathcal{H}}$) to be controlled exactly, while producing sufficiently chaotic motions to generate turbulence. While $\sigma_{\varepsilon} = \varepsilon_{\mathcal{H}}/\varepsilon$ is thus fixed, the imbalance $\sigma_c \approx \mathcal{H}/E$ is determined by the turbulence and evolves in time. Initial conditions are random and large-scale with energy $E = 10\varepsilon\tau_A$, where $\tau_A = L_z/v_A$ is the Alfvén crossing time. The perpendicular and parallel energy dissipation rates are $\varepsilon_{\perp}^{\text{diss}} = \nu_{6\perp} \sum_{k_{\perp}, k_z} k_{\perp}^6 E(k_{\perp}, k_z)$ and $\varepsilon_z^{\text{diss}} = \nu_{6z} \sum_{k_{\perp}, k_z} k_z^6 E(k_{\perp}, k_z)$, where $E(k_{\perp}, k_z)$ is the 2-D energy spectrum (in steady state, if it exists, we would have $\varepsilon = \varepsilon^{\text{diss}} = \varepsilon_{\perp}^{\text{diss}} + \varepsilon_z^{\text{diss}}$). Simulations are run across a range of resolutions up to $N_{\perp} = N_z = 2048$. For the highest-resolution cases, we use a recursive refinement procedure, restarting a lower-resolution case at twice the resolution and running until $\varepsilon_{\perp}^{\text{diss}}$ converges in time; this dramatically reduces the computational cost to enable otherwise unaffordable simulations. All simulations use $Z = 1$ and $\tau = 0.5$ (so that the ion-sound radius is equal to ρ_i).

[‡] It is worth commenting briefly on the recent work of Milanese *et al.* (2020), which has considered a similar system with a conserved energy and generalised helicity. In that system, the function $1/v_{\text{ph}}(k_{\perp})$ in the generalised helicity *increases* with k_{\perp} at large k_{\perp} , which is the opposite of our Eq. (2.9). This leads to the phenomenon of “dynamic phase alignment”, whereby fluctuations become increasingly correlated at small scales, reducing the strength of their nonlinear interaction so as to maintain constant fluxes of energy and helicity.

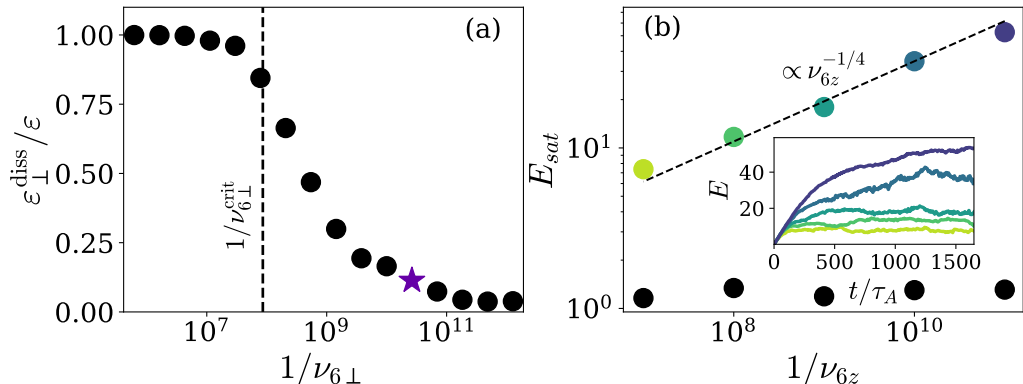


FIGURE 3. Panel (a) illustrates the violation of the zeroth law of turbulence with respect to the perpendicular dissipation. Each point shows $\varepsilon_{\perp}^{\text{diss}}/\varepsilon$ in the saturated state of an FLR-MHD simulation with a different value of $\nu_{6\perp}$. The simulations all have $\sigma_{\varepsilon} = 0.88$, $\rho_i = 0.02L_{\perp}$, $256 \leq N_{\perp} \leq 512$, $N_z = 256$, and are initialised from the saturated state of the simulation marked by the purple star and run until they reach steady state. The vertical dashed line shows the critical $\nu_{6\perp}$ at which the RMHD dissipation scale lies above the scale of the helicity barrier (see text), so that simulations with $1/\nu_{6\perp} < 1/\nu_{6\perp}^{\text{crit}}$ are ignorant of FLR effects (the turbulence is dissipated at larger scales), while those with $1/\nu_{6\perp} > 1/\nu_{6\perp}^{\text{crit}}$ are not. We see that the helicity barrier halts the perpendicular dissipation causing $\varepsilon_{\perp}^{\text{diss}} \ll \varepsilon$ at small $\nu_{6\perp}$. In panel (b), coloured points show the saturation energy E_{sat} versus parallel hyper-dissipation ν_{6z} for 5 FLR-MHD simulations with $N_{\perp} = 64$, $N_z \leq 256$, $\sigma_{\varepsilon} = 0.88$, and $\rho_i = 0.1L_{\perp}$. Equivalent RMHD simulations ($\rho_i = 0$) are shown with black points. The dependence of E_{sat} on ν_{6z} at fixed ε demonstrates that the helicity barrier causes the violation of the zeroth law of turbulence with respect to the parallel dissipation. The inset shows the time evolution of the energy in each case (colours match those of the points).

3.2. Results

Figure 3 demonstrates how imbalanced FLR-MHD turbulence violates the zeroth law of turbulence. Figure 3(a) shows the normalised perpendicular dissipation rate $\varepsilon_{\perp}^{\text{diss}}/\varepsilon$ in the saturated state of sixteen FLR-MHD simulations with $\sigma_{\varepsilon} = 0.88$, $\rho_i = 0.02L_{\perp}$, and varying perpendicular hyper-dissipation $\nu_{6\perp}$. The simulations have fixed ν_{6z} , resolution $N_{\perp} = N_z = 256$ (or $N_{\perp} = 512$ for the four lowest- $\nu_{6\perp}$ cases), and were run by restarting from the saturated state of the $1/\nu_{6\perp} \simeq 3 \times 10^{10}$ simulation (denoted by the purple star), which will be discussed in detail below. We see a precipitous drop in $\varepsilon_{\perp}^{\text{diss}}$ for $1/\nu_{6\perp} \gtrsim 10^8$, which signifies that the turbulent energy flux cannot proceed to small perpendicular scales for small $\nu_{6\perp}$. This is the signature of the helicity barrier predicted above in § 2.3.2: if the scale at which the energy dissipates due to $\nu_{6\perp}$ is such that the inequality (2.11) is violated, the constant perpendicular flux solution cannot hold.

The vertical dashed line in Fig. 3(a) shows the critical value $\nu_{6\perp}^{\text{crit}}$ needed to set the perpendicular dissipation scale of RMHD turbulence equal to the scale $k_{\perp}^{\text{crit}} \simeq 22.4(2\pi/L_{\perp})$ where $1/v_{\text{ph}}(k_{\perp}^{\text{crit}}) = \sigma_{\varepsilon} = 0.88$. We estimate $\nu_{6\perp}^{\text{crit}}$ from $\nu_{6\perp} k_{\perp}^6 \sim k_{\perp} Z_{k_{\perp}}^{-}$, where $Z_{k_{\perp}}^{-} \sim Z_0^{-}(k_{\perp} L_{\perp})^{-1/4}$ is the typical variation in Z^{-} across scale k_{\perp}^{-1} , and the outer-scale amplitude Z_0^{-} is taken from saturated state of the similar RMHD simulation shown in Fig. 5. If $\nu_{6\perp} > \nu_{6\perp}^{\text{crit}}$, the cascade can dissipate in the standard way on hyper-dissipation, setting up an imbalanced RMHD cascade; if $\nu_{6\perp} < \nu_{6\perp}^{\text{crit}}$, the inequality (2.11) applies, stopping the cascade before it reaches small perpendicular scales and causing $\varepsilon_{\perp}^{\text{diss}} \ll \varepsilon$.

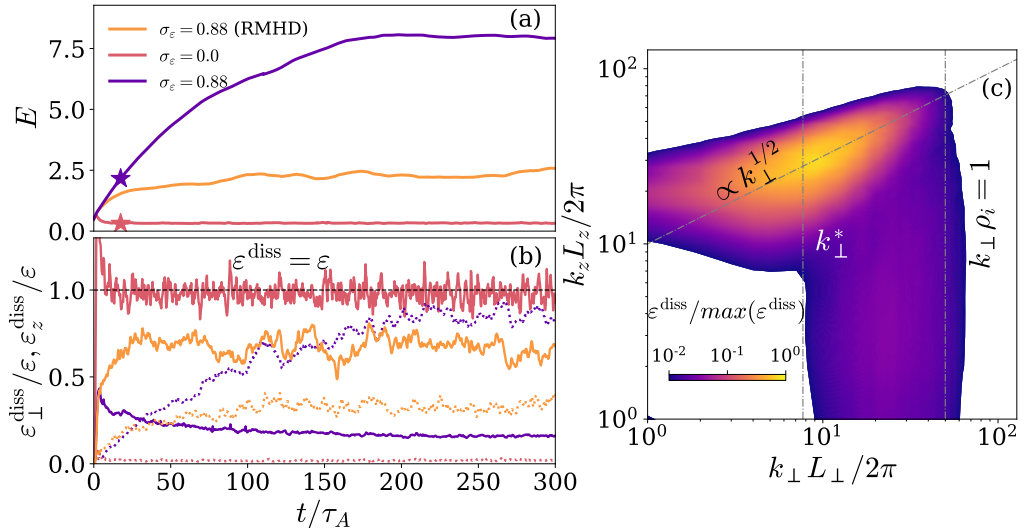


FIGURE 4. Energy and dissipation properties from a set of simulations at resolution $N_{\perp} = N_z = 256$. Panel (a) compares the time evolution of energy in imbalanced FLR-MHD ($\sigma_{\varepsilon} = 0.88$, $\rho_i = 0.02L$) to balanced FLR-MHD ($\sigma_{\varepsilon} = 0$, $\rho_i = 0.02L$) and imbalanced RMHD ($\sigma_{\varepsilon} = 0.88$, $\rho_i = 0$). The stars indicate the time from which the higher-resolution simulations of Figs. 1–2 were initialised. Panel (b) shows $\varepsilon_{\perp}^{\text{diss}}$ (solid lines) and $\varepsilon_z^{\text{diss}}$ (dotted lines) for each case, to show that saturation is reached through *parallel* dissipation (unlike in balanced turbulence and in imbalanced RMHD). Panel (c) shows the (k_{\perp}, k_z) dissipation spectrum in the saturated state of imbalanced FLR-MHD, illustrating that dissipation occurs primarily at the perpendicular break scale ($k_{\perp}^* \rho_i \simeq 0.15$) at high k_z .

This inability of the perpendicular cascade to process injected energy into perpendicular dissipation suggests that the *parallel* dissipation must play a role. This is surprising given that parallel dissipation is usually neglected in magnetised-turbulence theories because the increasing elongation of eddies at smaller scales generally implies $\varepsilon_{\perp}^{\text{diss}} \gg \varepsilon_z^{\text{diss}}$. In Fig. 3(b), we show the turbulent-energy saturation amplitude E_{sat} as a function of the parallel hyper-dissipation ν_{6z} . These simulations are again forced with injection imbalance $\sigma_{\varepsilon} = 0.88$ and use a lower resolution $N_{\perp} = 64$ and $64 \leq N_z \leq 256$ (with N_z chosen as appropriate for each ν_{6z}) because of the long saturation times. The perpendicular dissipation is fixed and sufficiently small for there to be a helicity barrier. We compare FLR-MHD turbulence with $\rho_i = 0.1L_{\perp}$ (coloured points) to RMHD turbulence ($\rho_i = 0$; black points) to demonstrate the significant role played by FLR effects. The difference is obvious: FLR-MHD turbulence saturates at much larger amplitudes, which increase with decreasing dissipation; larger amplitudes are associated with longer saturation times (see inset; cf. [Miloshevich et al. 2020](#)). This dependence of saturation time and large-scale properties on ν_{6z} shows that imbalanced FLR-MHD turbulence violates the zeroth law of turbulence with respect to the parallel, as well as the perpendicular, dissipation.

The implications of these findings are twofold. First, in order to saturate, imbalanced FLR-MHD turbulence must access small-scale parallel physics, escaping the ordering assumptions ($l_{\parallel} \gg l_{\perp}$) used to derive the FLR-MHD model in the first place. This suggests that detailed properties of the saturated state achieved by this model are not relevant to real physical systems. Secondly, when the helicity barrier halts the perpendicular cascade, the system does not develop a true parallel cascade that can process the energy and helicity input into parallel dissipation. Rather, its saturated

amplitude depends directly on the microphysical parallel dissipation (the specific $\sim \nu_{6z}^{-1/4}$ dependence is explained below), suggesting that in the limit of vanishing parallel dissipation, the turbulence would fail to saturate completely.

These highly unusual characteristics motivate a more thorough exploration of imbalanced FLR-MHD turbulence. Below and in Figs. 1–2, we present detailed simulation results to help explain the effect of the helicity barrier and its potential relevance to space plasmas. We compare imbalanced FLR-MHD to an equally imbalanced RMHD simulation and balanced FLR-MHD, all at the same ε . To aid discussion, we break the time evolution into three phases: first, a transient phase during which small-scale motions are produced from the initial conditions; next, a *pseudo-stationary phase*, which is the long phase of slow energy growth (seen in the inset of Fig. 3b) that occurs due to the helicity barrier; and finally, saturation, when $\varepsilon \approx \varepsilon_{\perp}^{\text{diss}} + \varepsilon_z^{\text{diss}}$ and $\partial_t E \approx 0$. During the pseudo-stationary phase and saturation, the helicity barrier creates a sharp break in the perpendicular spectrum at a wavenumber that we will denote k_{\perp}^* .

3.2.1. The effect of the helicity barrier

Figures 4–6 show the time evolution of the energy, dissipation $\varepsilon_{\perp,\parallel}^{\text{diss}}$, energy spectra $E^{\pm}(k_{\perp})$, and total energy flux $\Pi(k_{\perp})$, comparing imbalanced FLR-MHD at $\sigma_{\varepsilon} = 0.88$ and $\rho_i = 0.02L_{\perp}^{\dagger}$ with balanced FLR-MHD ($\sigma_{\varepsilon} = 0$, $\rho_i = 0.02L_{\perp}$) and imbalanced RMHD ($\sigma_{\varepsilon} = 0.88$, $\rho_i = 0$). These simulations, which have a resolution of $N_{\perp} = N_z = 256$, are used as low-resolution seeds (starting at $t \approx 18\tau_{A0}$) for the recursive resolution refinement that allows us to reach $N_{\perp} = N_z = 2048$ in Fig. 2 (the full time evolution is only computationally accessible at modest resolution). Let us first describe the balanced FLR-MHD and imbalanced RMHD cases in order to highlight the effect of the helicity barrier.

The balanced FLR-MHD simulation reaches saturation after a transient phase lasting several τ_A , exhibiting a $\sim k_{\perp}^{-3/2}$ spectrum at large scales (Fig. 5) and constant flux of energy to small scales (Fig. 6) where it is dissipated with $\varepsilon_{\perp}^{\text{diss}} \gg \varepsilon_z^{\text{diss}}$ (Fig. 4b). While the transition to KAW turbulence ($\sim k_{\perp}^{-2.8}$) at $k_{\perp}\rho_i \simeq 1$ is superseded by the dissipation range at $N_{\perp} = 256$, it is clearly visible in the $N_{\perp} = 2048$ spectrum in Fig. 2. The imbalanced RMHD simulation is similar, although it is slower to saturate, reaching steady state by $\tau_A \simeq 40$, with a $\sim k_{\perp}^{-3/2}$ spectrum in E^+ and E^- (Fig. 5) and energy fluxes to small perpendicular scales (not shown). The larger saturated energy arises because the cascade time τ_{cas} is larger in imbalanced turbulence due to its slower nonlinear interactions (Chandran 2008; Lithwick *et al.* 2007), implying $E_{\text{sat}} \sim \varepsilon\tau_{\text{cas}}$ is larger with fixed ε . As E grows, the parallel outer scale $l_{\parallel 0}$ decreases due to critical balance ($l_{\parallel 0} \sim L_{\perp}v_A/E^{1/2}$), which causes a modest parallel dissipation ($\varepsilon_z^{\text{diss}} \simeq 0.3\varepsilon^{\text{diss}}$) observed in RMHD for the chosen parameters (Fig. 4b). This disappears at either lower ε and/or higher resolution.

Imbalanced FLR-MHD turbulence is markedly different from both its balanced counterpart and imbalanced RMHD turbulence. As noted above, the latter is especially remarkable because FLR-MHD is identical to RMHD at $k_{\perp}\rho_i \ll 1$, and ρ_i (vertical line in Fig. 5) lies only slightly above the resolution cutoff (where perpendicular dissipation dominates) at these parameters. After an initial transient phase ($t \lesssim 5\tau_A$) when its evolution is similar to RMHD, the system forms a sharp spectral break at k_{\perp}^* , and the pseudo-stationary phase begins. During this phase, the outer-scale energy in $E^+(k_{\perp})$ grows in time, while the spectral break, which lies near $k_{\perp}^*\rho_i \simeq 1$ at early times, migrates to larger scales. That this break is due to the “helicity barrier” can be seen directly in

[†] The saturated state of this simulation is shown with the purple star in Fig. 3a.

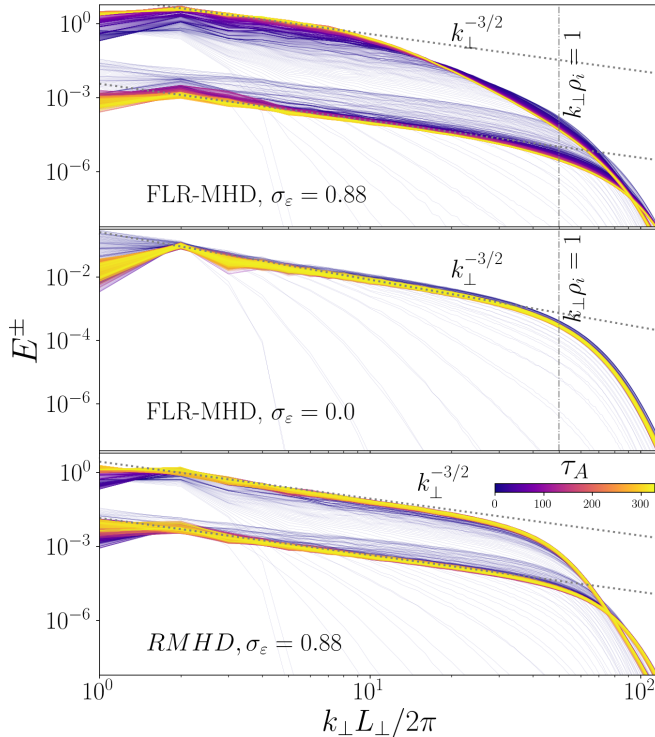


FIGURE 5. Time evolution of the spectra, $E^\pm(k_\perp)$, for the simulations shown in Fig. 4, comparing imbalanced FLR-MHD (top panel), balanced FLR-MHD (middle panel), and imbalanced RMHD (bottom panel). Individual spectra are shown at times spaced by $t = 0.1\tau_A$, as indicated by the colour. While the spectrum converges rapidly in balanced FLR-MHD and imbalanced RMHD turbulence, the spectra of imbalanced FLR-MHD turbulence continue to evolve until $t \simeq 200\tau_A$, with the break continuously moving to larger scales.

the energy flux (Fig. 6): as time goes on, $\Pi(k_\perp)$ is confined to increasingly large scales (broadly matching k_\perp^* , shown with coloured lines), as well as fluctuating wildly compared to balanced turbulence. Clearly, $\Pi \ll \varepsilon$ for $k_\perp > k_\perp^*$, which explains the continual increase in E with time during this phase. The subdominant mode’s spectrum $E^-(k_\perp)$ behaves quite differently to $E^+(k_\perp)$, undergoing a modest decrease at earlier times and saturating well before E^+ . This implies that the energy imbalance σ_ε increases with time during the pseudo-stationary phase. Interestingly, the E^- cascade appears agnostic to the break in $E^+(k_\perp)$ and proceeds to small perpendicular scales. This is consistent with the observation that the saturated perpendicular energy dissipation seems to approach $\varepsilon_\perp^{\text{diss}} \approx 2\varepsilon^- = \varepsilon(1 - \sigma_\varepsilon)$ in the pseudo-stationary phase (a result that has been confirmed at higher resolution and at other σ_ε). This suggests a form of “flux pinning” ($\varepsilon^- \approx \varepsilon^+$), whereby the energy flux to small scales is determined by the requirement of a near-balanced KAW cascade (as seen in Fig. 2), which thus avoids the problems associated with the inverse cascade of helicity. The amplitude of this cascade appears to be limited by the availability of Θ^- fluctuations arriving from the inertial range.†

The saturation mechanism in imbalanced FLR-MHD is fundamentally different to the

† As seen in Fig. 3(a) at small $\nu_{6\perp}$, this result ($\varepsilon_\perp^{\text{diss}} \approx 2\varepsilon^-$) does not hold in the *saturated* state of FLR-MHD turbulence. This is not unexpected, because the parallel dissipation that causes saturation by dissipating energy (see below) can dissipate Θ^- as well as Θ^+ , thus reducing the flux of energy to small perpendicular scales yet further.

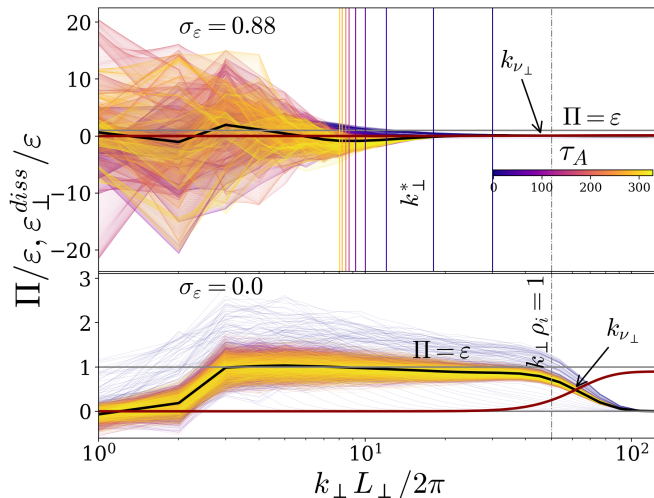


FIGURE 6. Time evolution of the normalised energy flux $\Pi(k_\perp)/\varepsilon$ for the simulations of Figs. 4–5, comparing imbalanced FLR-MHD (top panel) and balanced FLR-MHD (bottom panel). The colouring is the same as in Fig. 5. While balanced FLR-MHD turbulence shows the expected near-constant flux to small scales (where it is dissipated), imbalanced FLR-MHD turbulence is characterised by wild fluctuations in Π (note different ordinate scale and the position of the grey line at $\Pi = \varepsilon$), which, with time, are increasingly confined to large scales. The time-dependent wavenumber of the break (k_\perp^*) is shown with the coloured vertical lines. We also show, with k_{ν_\perp} , the scale at which Π is equal to the perpendicular dissipation flux (brown lines) in each simulation. The small flux $\Pi \ll \varepsilon$ at smaller scales provides direct evidence for the existence of the helicity barrier.

balanced case or to imbalanced RMHD turbulence, because $\Pi(k_\perp)$ at $k_\perp \gtrsim k_\perp^*$ remains limited to $\simeq 2\varepsilon^-$, no matter what the turbulence amplitude. Saturation finally occurs—at $t \approx 200\tau_A$ with energy imbalance reaching $\sigma_\varepsilon \approx 0.999$ for the FLR-MHD simulation of Figs. 4–6—once eddies of perpendicular scale k_\perp^* reach sufficiently large amplitudes and small parallel scales to dissipate through *parallel* hyper-dissipation (Fig. 4). Our simulations indicate that this generation of small parallel scales occurs due to critical balance rather than through an independent parallel cascade to small l_\parallel at fixed k_\perp (which would imply a ν_{6z} -independent E_{sat}). We can thus estimate the saturation amplitude using $l_\parallel(k_\perp) \sim l_{\parallel 0}(L_\perp k_\perp)^{-1/2}$ and $Z_{k_\perp}^+ \sim E^{1/2}(L_\perp k_\perp)^{-1/4}$, where $Z_{k_\perp}^+$ is the typical variation in Z^+ across scale k_\perp^{-1} and $l_\parallel(k_\perp)$ is the corresponding parallel correlation length (Mallet & Schekochihin 2017). Noting that saturation occurs at $\nu_{6z} l_\parallel (k_\perp^*)^{-6} (Z_{k_\perp^*}^+)^2 \sim \varepsilon$ and $l_{\parallel 0} \sim L_\perp v_A / E_{\text{sat}}^{1/2}$, we find

$$E_{\text{sat}} \sim (\varepsilon / \nu_{6z})^{-1/4} (k_\perp^* L_\perp)^{-5/8} (v_A L_\perp)^{3/2}. \quad (3.1)$$

The $\nu_{6z}^{-1/4}$ scaling is approximately satisfied by the simulations in Fig. 3 (which all saturate with similar k_\perp^* near the forcing scales), while the 2-D dissipation spectrum in Fig. 4c confirms directly that most dissipation occurs at small l_\parallel on k_\perp^* -scale eddies. Figure 4c also shows the critical-balance scaling $l_\parallel \sim k_\perp^{-1/2}$ (although note that k_z rather than $k_\parallel \sim l_\parallel^{-1}$ is plotted) and the finite $\varepsilon_\perp^{\text{diss}}$ at larger k_\perp from flux leakage through the barrier. As mentioned above, this saturation mechanism is unphysical: by growing to $\varepsilon_z^{\text{diss}} > \varepsilon_\perp^{\text{diss}}$, the system is trying to break the $l_\parallel \ll l_\perp$ ordering used to derive FLR-MHD. Nonetheless, only with this basic understanding of why the system saturates can we evaluate how the helicity barrier might evolve in more realistic scenarios.

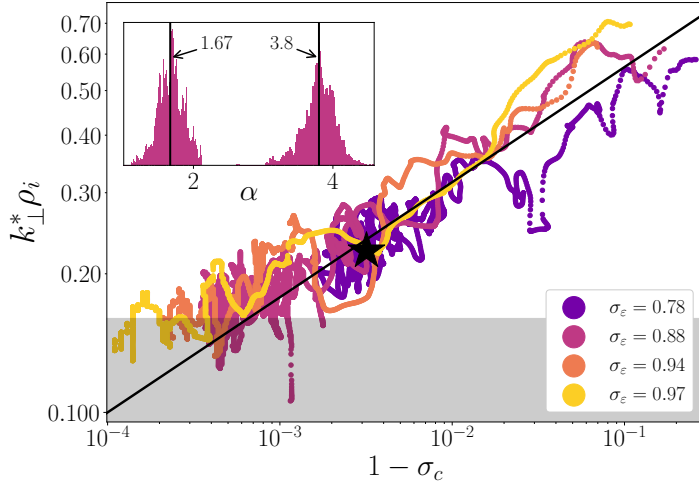


FIGURE 7. Position of the break $k_{\perp}^* \rho_i$ versus the energy imbalance $(1 - \sigma_c)$ for a number of $N_{\perp} = N_z = 256$ simulations with different injection imbalances σ_{ε} . As $\sigma_c(t)$ grows in time due to the helicity barrier, there is concurrent decrease in k_{\perp}^* , with no obvious dependence on the helicity injection $\sigma_{\varepsilon} = \varepsilon_{\mathcal{H}}/\varepsilon$ or other time dependence. The black line shows the empirical fit (3.2), the star shows the fit for Fig. 2, and the greyed out region indicates where k_{\perp}^* gets within a factor of 2 of the forcing scale ($k_{\perp}^* < 4 \times 2\pi/L$). The inset shows a histogram of the fitted spectral slope $\sim k_{\perp}^{-\alpha}$ above and below the break for the $\sigma_{\varepsilon} = 0.88$ simulation of Fig. 5 (the averages are $\langle \alpha \rangle \approx 1.67$ above the break and $\langle \alpha \rangle \approx 3.8$ below the break).

Finally, it is worth noting an interesting feature of the MHD-scale ($k_{\perp} < k_{\perp}^*$) turbulence in the pseudo-stationary phase: even though most of the energy input is unable to be thermalised during this phase, causing E^+ to grow in time, the spectrum remains approximately $E^+(k_{\perp}) \sim k_{\perp}^{-3/2}$ for $k_{\perp} < k_{\perp}^*$ (see Fig. 2 and Fig. 7 inset). This is in contrast to standard (e.g., hydrodynamic) turbulence with insufficient small-scale dissipation, which usually forms a thermal spectrum that is an increasing function of k_{\perp} (see e.g., Cichowlas *et al.* 2005; Frisch *et al.* 2008, for a study of the truncated Euler equations). We speculate that this occurs because, even in the presence of a helicity barrier, Θ^- still nonlinearly cascades to dissipate at small scales (see discussion above), thus behaving in a way similar to RMHD. But, for $k_{\perp} \rho_i < 1$ where $\mathbf{Z}^- \approx \hat{\mathbf{z}} \times \nabla_{\perp} \Theta^-$, the nonlinear cascade of Θ^+ is governed by Θ^- because only counter-propagating waves interact in RMHD. This suggests that E^+ does not form a thermal spectrum because of the Θ^- cascade, although the phenomenology of the cascade in the presence of a barrier remains highly uncertain. Nonetheless, our simulations robustly show that both $E^+(k_{\perp})$ and $E^-(k_{\perp})$ scale as $\sim k_{\perp}^{-3/2}$, as observed in the solar wind (Chen 2016; Chen *et al.* 2020).

3.2.2. The ion spectral break

For testing of the helicity-barrier hypothesis against observations, it is of interest to understand the position and spectral slope of the ion-kinetic transition region around ρ_i scales. Given the unphysical saturation mechanism in our simulations, we hypothesise that the “pseudo-stationary” phase is of more relevance to realistic space plasmas and that the “instantaneous” state of turbulence during that stage can be characterised by the energy imbalance $\sigma_c(t)$ and the injection imbalance σ_{ε} , i.e., that the time history of the growth is unimportant. Figure 7 shows $k_{\perp}^* \rho_i$ versus imbalance $(1 - \sigma_c)$ for simulations

with four different σ_ε at $N_\perp = N_z = 256$, as well as the spectral slopes ($\sim k_\perp^{-\alpha}$) above and below k_\perp^* for $\sigma_\varepsilon = 0.88$ (inset; the values of α are obtained via a broken-power-law fit; [Astropy Collaboration 2013](#)). We see good correlation of k_\perp^* to $\sigma_c(t)$, approximately

$$k_\perp^* \rho_i \simeq (1 - \sigma_c)^{1/4}, \quad (3.2)$$

with little dependence on the injected flux. We have also confirmed that the 1/4-power scaling (although not the numerical coefficient) is robust to the order of the parallel hyper-dissipation (it also holds if $\nu_{6z} = 0$; not shown). Spectral slopes in the ion-kinetic transition range ($k_\perp > k_\perp^*$) are seen to vary more than in the MHD range ($k_\perp < k_\perp^*$) and are very steep, $\alpha \simeq 4$, in good agreement with PSP observations ([Bowen et al. 2020a](#)).

4. Discussion

Our simulations show a dramatic difference in imbalanced Alfvénic turbulence depending on whether or not energy can be dissipated at spatial scales above the ion-gyroradius scale. If it can, turbulence proceeds in a relatively conventional way, with energy reaching small perpendicular scales where it is thermalised by (hyper)-dissipation. If it cannot, the helicity barrier blocks the cascade at $k_\perp^* \rho_i \lesssim 1$, only a small proportion ($\simeq 2\varepsilon^-$) of the energy can reach the smallest perpendicular scales where it would heat electrons, while E^+ grows with time until it becomes so large that modes at k_\perp^* (which itself moves to large scales) dissipate on the parallel viscosity. The latter effect is unphysical—FLR-MHD is derived by assuming $l_\parallel \gg l_\perp$ —so the obvious question that arises is what would happen in a real plasma such as the solar wind. In order for the barrier to lose its importance for large-scale dynamics, some mechanism must either remove nearly all of the helicity in the system, thus allowing the energy to be channelled into the small-scale KAW cascade, or significantly dissipate both energy and helicity at or above the scale of the barrier (as the parallel dissipation does in FLR-MHD). Presumably a real plasma will find a way to accomplish one of these feats—the question is which, and what conditions (e.g., fluctuation amplitudes) are required for it to do so. A definitive answer will have to wait either for observations or for high-resolution six-dimensional kinetic simulations, but we can nonetheless speculate on possibilities.

The first possibility is that there exists another perpendicular dissipation mechanism that stops the formation of a helicity barrier in the first place. Within the gyrokinetic ordering $l_\perp \ll l_\parallel$, because the low ion-thermal speed at $\beta_i \ll 1$ implies that Alfvénic energy is incapable of heating ions significantly at any scale, there are in principle three possible such mechanisms: electron Landau damping, electron-inertial effects, and interactions with the compressive cascade. Electron Landau damping is modest at $k_\perp \rho_i \sim 1$ when $1 \gg \beta \gg m_e/m_i$ (e.g., normalised damping of $\simeq 1\%$ at $\beta \simeq 0.1$; see [Howes et al. 2006](#)), while electron-inertial effects change the equations only once $k_\perp d_e \sim 1$; so, neither of these effects seems capable of damping substantial helicity or energy. A compressive cascade, although it cannot exchange energy with Alfvénic motions ([Schekochihin et al. 2019](#)), does break helicity conservation around $k_\perp \rho_i \sim 1$; however, in order to have a significant effect, the compressive and Alfvénic cascades must have similar energy contents, which is not generally observed in the solar wind ([Bruno & Carbone 2013](#); [Chen 2016](#); [Chen et al. 2020](#)). Beyond gyrokinetics, cyclotron damping, although perhaps important in the KAW range ([Arzamasskiy et al. 2019](#)), requires Larmor-frequency fluctuations, a requirement that is difficult to reach for $k_\perp \rho_i \lesssim 1$ fluctuations with $l_\parallel \ll \rho_i$. Stochastic-ion heating ([Chandran et al. 2010](#)) is more promising—it can dissipate significant turbulent energy at $k_\perp \rho_i \sim 1$ so long as the fluctuation amplitude there exceeds a critical threshold $\simeq 0.2\beta^{1/2}$ —perhaps acting as a dissipation “switch” as

the amplitude grows. It is worth noting, however, that if a $k_{\perp}^* \rho_i \lesssim 1$ barrier has formed before significant stochastic heating occurs, this reduces the ρ_i -scale turbulence amplitude substantially, which also reduces the heating efficiency.

If the aforementioned perpendicular dissipation mechanisms fail to dissolve the barrier, it is also possible that—even in a real plasma—large-scale energy cannot dissipate, either growing until significant power reaches small parallel scales (of order d_i or ρ_i) or, in stratified environments such as the solar wind (Chandran & Perez 2019), propagating and growing without dissipation until wave reflection causes the imbalance to decrease enough to allow the cascade to proceed. In the former case, various other, non-gyrokinetic dissipation avenues are made available to the plasma; for example, other cascade channels (Saito *et al.* 2008; Meyrand & Galtier 2012) and ion-cyclotron damping, which could absorb the cascade’s energy (much like the parallel hyper-dissipation in our simulations). Interestingly, PSP has observed surprisingly high power in $l_{\parallel} \sim \rho_i$ ion-cyclotron waves (Huang *et al.* 2020; Bowen *et al.* 2020b), which may be a signature of this mechanism. Further, Duan *et al.* (2021) find a sharp drop in the wavevector anisotropy $l_{\parallel}(l_{\perp})$ around the break scale, indicating that the dynamics are generating small parallel scales faster than small perpendicular scales. Finally, magnetic reconnection may play an important role by enabling nonlocal energy or helicity transfers (Mallet *et al.* 2017; Loureiro & Boldyrev 2017; Vech *et al.* 2018); although reconnection is possible within FLR-MHD, it is necessary to include electron-inertial effects to capture this physics properly.

4.1. A critical imbalance?

Our theoretical arguments for helicity-barrier formation, which relied on conservation of energy and helicity in FLR-MHD, suggest that a barrier should form with *any* injected imbalance σ_{ε} , but with the constant flux solution failing at smaller scales for smaller σ_{ε} , *viz.*, for $1/v_{\text{ph}}(k_{\perp}) < \sigma_{\varepsilon}$.[†] We have confirmed this prediction numerically down to $\sigma_{\varepsilon} \simeq 0.3$ (not shown). It is challenging to observe at yet smaller σ_{ε} , both because very small scales (compared to ρ_i) must be resolved, and because a large proportion of the energy flux ($\simeq 2\varepsilon^-$) is not affected by the barrier, making the resulting growth in energy rather slow. It is, however, clear that non-FLR-MHD effects will give rise to a critical σ_{ε} , below which there is no barrier. FLR-MHD breaks down at d_e scales and helicity is no longer conserved, implying that the helicity barrier will likely not form if

$$\sigma_{\varepsilon} \lesssim \frac{1}{v_{\text{ph}}(d_e^{-1})} \sim \frac{d_e}{\rho_i} = \frac{Z}{\sqrt{\tau}} \sqrt{\frac{m_e}{m_i}} \beta_e^{-1/2} \quad (4.1)$$

(the latter estimates assume $\beta_e \gg m_e/m_i$). The discussion of the previous paragraph also suggests that other effects (e.g., stochastic-ion heating) would further increase the minimal σ_{ε} for which the barrier forms, by dissipating some helicity or energy. Measurement of this critical imbalance, along with improved theoretical understanding of helicity-barrier formation and dissolution, is left to future studies.

4.2. Implications for the solar wind

The qualitative agreement of our FLR-MHD energy spectra with those observed in the solar wind is highly suggestive. As far as we are aware, no previous numerical simulations have been able to produce similar double-kinked spectra. The position, shape, and cause of the ion-kinetic transition has been a decades-long puzzle with numerous proposed

[†] Note that this is not incompatible with the observation of Fig. 7 that the break is independent of σ_{ε} : once the barrier forms, the system is under no obligation to have a constant flux above the break, meaning the flux can go to zero at scales *above* where $\sigma_{\varepsilon} v_{\text{ph}}(k_{\perp}) \simeq 1$.

explanations (Schekochihin *et al.* 2009; Sahraoui *et al.* 2010; Meyrand & Galtier 2012; Lion *et al.* 2016; Voitenko & De Keyser 2016; Mallet *et al.* 2017; Woodham *et al.* 2018); observations show widely varying break positions and slopes (Leamon *et al.* 1998) often followed by a spectral flattening at yet smaller scales (Sahraoui *et al.* 2009; Bowen *et al.* 2020a; Duan *et al.* 2021). In addition, larger-scale transitions to steeper spectra correlate with higher-amplitude fluctuations, lower β , higher proton-scale magnetic helicity, and fast-wind regions (Smith *et al.* 2006; Bruno *et al.* 2014; Vech *et al.* 2018; Zhao *et al.* 2020), the latter of which is known to be more imbalanced than the slow wind. Each of these observations is well explained by the helicity-barrier hypothesis, at least qualitatively: we reproduce double-kinked spectra with the first break at a non-universal scale above $k_{\perp}\rho_i = 1$, while steeper spectra and larger-scale breaks result from the energy growing in time (Fig. 5). It is also worth noting that direct measurement of the turbulent energy flux in the solar wind has found the surprising result that the Z^+ flux seems to reverse at large imbalance (Smith *et al.* 2009); although not fully explained by our simulations (given that our forcing injects energy only at large scales), the result does indicate the presence of a critical imbalance that controls key features of the cascade. Future observations, combined with more realistic simulations, will provide more stringent tests of the theory.

More generally, if the helicity barrier proves to be a robust feature of plasma turbulence, we see a number of interesting implications. Turbulence is believed to contribute importantly to solar-wind heating (Dmitruk *et al.* 2002), so the requirement that it build up significantly in amplitude before being able to dissipate may have consequences for global heliospheric models (Verdini & Velli 2007; Chandran & Hollweg 2009). It is also interesting to ask about the plausible relevance to the sudden large-scale field reversals, or “switchbacks,” observed ubiquitously by PSP (Kasper *et al.* 2019; Bale *et al.* 2019): if switchbacks form *in-situ* due to wave growth in the expanding plasma (Squire *et al.* 2020), their existence relies on the dominance of growth over dissipation through turbulence. Halting energy dissipation via the helicity barrier could thus favor the development of sharp, large-amplitude structures, as observed. Finally, and more generally, the helicity barrier reveals yet another way that weakly collisional plasmas confound standard intuition about their thermodynamics. While Joule found that water or mercury possess a well-defined heat capacity, independent of how the fluid is heated, heating of ions and electrons in a plasma depends not just on bulk properties such as T_e/T_i or β (Howes *et al.* 2008; Kawazura *et al.* 2019), but also, quite sensitively, on how it is stirred. While the influence of the driving compressibility on heating is already known (Schekochihin *et al.* 2019; Kawazura *et al.* 2020), we see that driving imbalance should also have a strong effect, by halting the flow of Alfvénic energy to electron scales. The helicity barrier is thus expected to narrow yet further the range of plasma conditions under which electrons are heated preferentially to ions.

Support for R.M. and J.S. was provided by Rutherford Discovery Fellowship RDF-U001804 and Marsden Fund grant UOO1727, which are managed through the Royal Society Te Apārangi. The work of A.A.S. was supported in part by the UK EPSRC programme grant EP/R034737/10. W.D. was supported by the US Department of Energy through grant DE-FG02-93ER-54197. The authors wish to acknowledge the use of New Zealand eScience Infrastructure (NeSI) high performance computing facilities and consulting support as part of this research. This work was partially performed using HPC resources from GENCI-CINES (Grant 2019-A0060510871). The authors report no conflict of interest.

REFERENCES

- ALEXAKIS, A. & BIFERALE, L. 2018 Cascades and transitions in turbulent flows. *Phys. Rep.* **767**, 1–101.
- ALEXANDROVA, O., LACOMBE, C., MANGENEY, A., GRAPPIN, R. & MAKSIMOVIC, M. 2012 Solar wind turbulent spectrum at plasma kinetic scales. *Astrophys. J.* **760**, 121.
- ALEXANDROVA, O., SAUR, J., LACOMBE, C., MANGENEY, A., MITCHELL, J., SCHWARTZ, S. J. & ROBERT, P. 2009 Universality of solar-wind turbulent spectrum from mhd to electron scales. *Phys. Rev. Lett.* **103** (16), 165003.
- ARZAMASSKIY, L., KUNZ, M. W., CHANDRAN, B. D. G. & QUATAERT, E. 2019 Hybrid-kinetic simulations of ion heating in Alfvénic turbulence. *Astrophys. J.* **879** (1), 53.
- ASTROPY COLLABORATION 2013 Astropy: A community python package for astronomy. *Astron. Astro.* **558**, A33.
- BALE, S. D., BADMAN, S. T., BONNELL, J. W. *et al.* 2019 Highly structured slow solar wind emerging from an equatorial coronal hole. *Nature* **576**, 237–242.
- BERESNYAK, A. 2014 Spectra of strong magnetohydrodynamic turbulence from high-resolution simulations. *Astrophys. J. Lett.* **784** (2), L20.
- BERESNYAK, A. & LAZARIAN, A. 2009 Structure of stationary strong imbalanced turbulence. *Astrophys. J.* **702** (1), 460–471.
- BOLDYREV, S. 2006 Spectrum of magnetohydrodynamic turbulence. *Phys. Rev. Lett.* **96**, 115002.
- BOLDYREV, S., HORAITES, K., XIA, Q. & PEREZ, J. C. 2013 Toward a theory of astrophysical plasma turbulence at subproton scales. *Astrophys. J.* **777** (1), 41.
- BOWEN, T. A., MALLET, A., BALE, S. D. *et al.* 2020a Constraining ion-scale heating and spectral energy transfer in observations of plasma turbulence. *Phys. Rev. Lett.* **125** (2), 025102.
- BOWEN, T. A., MALLET, A., HUANG, J. *et al.* 2020b Ion-scale electromagnetic waves in the inner heliosphere. *Astrophys. J. Supp.* **246** (2), 66.
- BRUNO, R. & CARBONE, V. 2013 The solar wind as a turbulence laboratory. *Living Rev. Solar Phys.* **10** (1), 2.
- BRUNO, R., TRENCHI, L. & TELLONI, D. 2014 Spectral slope variation at proton scales from fast to slow solar wind. *Astrophys. J. Lett.* **793** (1), L15.
- CHANDRAN, B. D. G. 2008 Strong anisotropic MHD turbulence with cross helicity. *Astrophys. J.* **685** (1), 646–658.
- CHANDRAN, B. D. G. & HOLLWEG, J. V. 2009 Alfvén wave reflection and turbulent heating in the solar wind from 1 solar radius to 1 AU: An analytical treatment. *Astrophys. J.* **707** (2), 1659–1667.
- CHANDRAN, B. D. G., LI, B., ROGERS, B. N., QUATAERT, E. & GERMASCHEWSKI, K. 2010 Perpendicular ion heating by low-frequency Alfvén-wave turbulence in the solar wind. *Astrophys. J.* **720** (1), 503–515.
- CHANDRAN, B. D. G. & PEREZ, J. C. 2019 Reflection-driven magnetohydrodynamic turbulence in the solar atmosphere and solar wind. *J. Plasma Phys.* **85** (4), 905850409.
- CHEN, C. H. K. 2016 Recent progress in astrophysical plasma turbulence from solar wind observations. *J. Plasma Phys.* **82** (6), 535820602.
- CHEN, C. H. K., BALE, S. D., BONNELL, J. W. *et al.* 2020 The evolution and role of solar wind turbulence in the inner heliosphere. *Astrophys. J. Supp.* **246** (2), 53.
- CHEN, C. H. K., MALLET, A., YOUSEF, T. A., SCHEKOCHIHIN, A. A. & HORBURY, T. S. 2011 Anisotropy of Alfvénic turbulence in the solar wind and numerical simulations. *Mon. Not. R. Astron. Soc.* **415** (4), 3219–3226.
- CHO, J. 2011 Magnetic helicity conservation and inverse energy cascade in electron magnetohydrodynamic wave packets. *Phys. Rev. Lett.* **106** (19), 191104.
- CICHOWLAS, C., BONAÏTI, P., DEBBASCH, F. & BRACHET, M. 2005 Effective dissipation and turbulence in spectrally truncated Euler flows. *Phys. Rev. Lett.* **95** (26), 264502.
- DMITRUK, P., MATTHAEUS, W. H., MILANO, L. J., OUGHTON, S., ZANK, G. P. & MULLAN, D. J. 2002 Coronal heating distribution due to low-frequency, wave-driven turbulence. *Astrophys. J.* **575** (1), 571–577.
- DOBROWOLNY, M., MANGENEY, A. & VELTRI, P. 1980 Fully developed anisotropic hydromagnetic turbulence in interplanetary space. *Phys. Rev. Lett.* **45** (2), 144–147.

- DUAN, D., HE, J., BOWEN, T. A., WOODHAM, L. D., WANG, T., CHEN, C. H. K., MALLET, A. & BALE, S. D. 2021 Anisotropy of solar-wind turbulence in the inner heliosphere at kinetic scales: PSP observations. *arXiv:2102.13294* .
- ELSASSER, W. M. 1950 The hydromagnetic equations. *Phys. Rev.* **79** (1), 183–183.
- FJØRTOFT, R. 1953 On the changes in the spectral distribution of kinetic energy for twodimensional, nondivergent flow. *Tellus* **5** (3), 225.
- FRISCH, U., KURIEN, S., PANDIT, R., PAULS, W., RAY, S. S., WIRTH, A. & ZHU, J.-Z. 2008 Hyperviscosity, Galerkin truncation, and bottlenecks in turbulence. *Phys. Rev. Lett.* **101**, 144501.
- GOLDREICH, P. & SRIDHAR, S. 1995 Toward a theory of interstellar turbulence. Strong Alfvénic turbulence. *Astrophys. J.* **438**, 763–775.
- HOWES, G. G., COWLEY, S. C., DORLAND, W., HAMMETT, G. W., QUATAERT, E. & SCHEKOCHIHIN, A. A. 2008 A model of turbulence in magnetized plasmas: Implications for the dissipation range in the solar wind. *J. Geophys. Res.: Space Phys.* **113** (A), A05103.
- HOWES, G. G., COWLEY, S. C., DORLAND, W., HAMMETT, G. W., QUATAERT, E. & SCHEKOCHIHIN, A. E. A. 2006 Astrophysical gyrokinetics: Basic equations and linear theory. *Astrophys. J.* **651** (1), 590–614.
- HOWES, G. G., DORLAND, W., COWLEY, S. C., HAMMETT, G. W., QUATAERT, E., SCHEKOCHIHIN, A. A. & TATSUNO, T. 2008 Kinetic simulations of magnetized turbulence in astrophysical plasmas. *Phys. Rev. Lett.* **100** (6), 065004.
- HUANG, S. Y., ZHANG, J., SAHRAOUI, F. *et al.* 2020 Kinetic scale slow solar wind turbulence in the inner heliosphere: Coexistence of kinetic Alfvén waves and Alfvén ion cyclotron waves. *Astrophys. J. Lett.* **897** (1), L3.
- JOULE, J. T. 1850 On the mechanical equivalent of heat. *Phil. Trans. R. Soc. London* **140**, 61–82.
- KASPER, J. C., BALE, S. D., BELCHER, J. W. *et al.* 2019 Alfvénic velocity spikes and rotational flows in the near-sun solar wind. *Nature* **576**, 228–231.
- KAWAZURA, Y., BARNES, M. & SCHEKOCHIHIN, A. A. 2019 Thermal disequilibrium of ions and electrons by collisionless plasma turbulence. *Proc. Nat. Acc. Sci.* **116** (3), 771–776.
- KAWAZURA, Y., SCHEKOCHIHIN, A. A., BARNES, M., TENBARGE, J. M., TONG, Y., KLEIN, K. G. & DORLAND, W. 2020 Ion versus electron heating in compressively driven astrophysical gyrokinetic turbulence. *Phys. Rev. X* **10** (4), 041050.
- KIM, H. & CHO, J. 2015 Inverse cascade in imbalanced electron magnetohydrodynamic turbulence. *Astrophys. J.* **801** (2), 75.
- LEAMON, R. J., SMITH, C. W., NESS, N. F., MATTHAEUS, W. H. & WONG, H. K. 1998 Observational constraints on the dynamics of the interplanetary magnetic field dissipation range. *J. Geophys. Res.* **103** (A3), 4775–4788.
- LION, S., ALEXANDROVA, O. & ZASLAVSKY, A. 2016 Coherent events and spectral shape at ion kinetic scales in the fast solar wind turbulence. *Astrophys. J.* **824** (1), 47.
- LITHWICK, Y., GOLDREICH, P. & SRIDHAR, S. 2007 Imbalanced strong MHD turbulence. *Astrophys. J.* **655** (1), 269–274.
- LOUREIRO, N. F. & BOLDYREV, S. 2017 Collisionless reconnection in magnetohydrodynamic and kinetic turbulence. *Astrophys. J.* **850** (2), 182.
- MALLET, A. & SCHEKOCHIHIN, A. A. 2017 A statistical model of three-dimensional anisotropy and intermittency in strong alfvénic turbulence. *Mon. Not. R. Astron. Soc.* **466** (4), 3918–3927.
- MALLET, A., SCHEKOCHIHIN, A. A. & CHANDRAN, B. D. G. 2017 Disruption of Alfvénic turbulence by magnetic reconnection in a collisionless plasma. *J. Plasma Phys.* **83** (6), 905830609.
- MARON, J. & GOLDREICH, P. 2001 Simulations of incompressible magnetohydrodynamic turbulence. *Astrophys. J.* **554** (2), 1175–1196.
- MCMANUS, M. D., BOWEN, T. A., MALLET, A. *et al.* 2020 Cross helicity reversals in magnetic switchbacks. *Astrophys. J. Supp.* **246** (2), 67.
- MEYRAND, R. & GALTIER, S. 2012 Spontaneous chiral symmetry breaking of Hall magnetohydrodynamic turbulence. *Phys. Rev. Lett.* **109**, 194501.
- MEYRAND, R., KANEKAR, A., DORLAND, W. & SCHEKOCHIHIN, A. A. 2019 Fluidization of collisionless plasma turbulence. *Proc. Nat. Acc. Sci.* **116** (4), 1185–1194.

- MILANESE, L. M., LOUREIRO, N. F., DASCHNER, M. & BOLDYREV, S. 2020 Dynamic phase alignment in inertial Alfvén turbulence. *Phys. Rev. Lett.* **125** (26), 265101.
- MILOSHEVICH, G., LAVEDER, D., PASSOT, T. & SULEM, P.-L. 2020 Inverse cascade and magnetic vortices in kinetic Alfvén-wave turbulence. *arXiv:2007.06976* .
- OUGHTON, S., PRIEST, E. R. & MATTHAEUS, W. H. 1994 The influence of a mean magnetic field on three-dimensional magnetohydrodynamic turbulence. *J. Fluid Mech.* **280**, 95–117.
- PASSOT, T., SULEM, P. L. & TASSI, E. 2018 Gyrofluid modeling and phenomenology of low- β_e Alfvén wave turbulence. *Phys. Plasmas* **25** (4), 042107.
- PEARSON, B. R., YOUSEF, T. A., HAUGEN, N. E. L., BRANDENBURG, A. & KROGSTAD, P.-Å. 2004 Delayed correlation between turbulent energy injection and dissipation. *Phys. Rev. E* **70** (5), 056301.
- PEREZ, J. C. & BOLDYREV, S. 2009 Role of cross-helicity in magnetohydrodynamic turbulence. *Phys. Rev. Lett.* .
- PEREZ, J. C., MASON, J., BOLDYREV, S. & CATTANEO, F. 2012 On the energy spectrum of strong magnetohydrodynamic turbulence. *Phys. Rev. X* **2**, 041005.
- POUQUET, A., STAWARZ, J. E. & ROSENBERG, D. 2020 Coupling large eddies and waves in turbulence: Case study of magnetic helicity at the ion inertial scale. *Atmosphere* **11** (2), 203.
- SAHRAOUI, F., GOLDSTEIN, M. L., BELMONT, G., CANU, P. & REZEAU, L. 2010 Three dimensional anisotropic k spectra of turbulence at subproton scales in the solar wind. *Phys. Rev. Lett.* **105**, 131101.
- SAHRAOUI, F., GOLDSTEIN, M. L., ROBERT, P. & KHOTYAINTEV, Y. V. 2009 Evidence of a cascade and dissipation of solar-wind turbulence at the electron gyroscale. *Phys. Rev. Lett.* **102** (23), 231102.
- SAITO, S., GARY, S. P., LI, H. & NARITA, Y. 2008 Whistler turbulence: Particle-in-cell simulations. *Phys. Plasmas* **15** (10), 102305.
- SCHEKOCHIHIN, A. A. 2020 MHD turbulence: A biased review. *arXiv:2010.00699* .
- SCHEKOCHIHIN, A. A., COWLEY, S. C., DORLAND, W., HAMMETT, G. W., HOWES, G. G., QUATAERT, E. & TATSUNO, T. 2009 Astrophysical gyrokinetics: Kinetic and fluid turbulent cascades in magnetized weakly collisional plasmas. *Astrophys. J. Supp.* **182** (1), 310.
- SCHEKOCHIHIN, A. A., KAWAZURA, Y. & BARNES, M. A. 2019 Constraints on ion versus electron heating by plasma turbulence at low beta. *J. Plasma Phys.* **85** (3), 905850303.
- SMITH, C. W., HAMILTON, K., VASQUEZ, B. J. & LEAMON, R. J. 2006 Dependence of the dissipation range spectrum of interplanetary magnetic fluctuations on the rate of energy cascade. *Astrophys. J. Lett.* **645** (1), L85–L88.
- SMITH, C. W., STAWARZ, J. E., VASQUEZ, B. J., FORMAN, M. A. & MACBRIDE, B. T. 2009 Turbulent cascade at 1 au in high cross-helicity flows. *Phys. Rev. Lett.* **103** (20), 201101.
- SQUIRE, J., CHANDRAN, B. D. G. & MEYRAND, R. 2020 In-situ switchback formation in the expanding solar wind. *Astrophys. J. Lett.* **891** (1), L2.
- STRAUSS, H. R. 1976 Nonlinear, three-dimensional magnetohydrodynamics of noncircular tokamaks. *Phys. Fluids* **19** (1), 134–140.
- TEACA, B., VERMA, M. K., KNAEPEN, B. & CARATI, D. 2009 Energy transfer in anisotropic magnetohydrodynamic turbulence. *Phys. Rev. E* **79**, 046312.
- VECH, D., MALLET, A., KLEIN, K. G. & KASPER, J. C. 2018 Magnetic reconnection may control the ion-scale spectral break of solar wind turbulence. *Astrophys. J. Lett.* **855** (2), L27.
- VELLI, M. 1993 On the propagation of ideal, linear Alfvén waves in radially stratified stellar atmospheres and winds. *Astron. Astro.* **270**, 304–314.
- VERDINI, A. & VELLI, M. 2007 Alfvén waves and turbulence in the solar atmosphere and solar wind. *Astrophys. J.* **662** (1), 669–676.
- VOITENKO, Y. & DE KEYSER, J. 2016 MHD-kinetic transition in imbalanced Alfvénic turbulence. *Astrophys. J. Lett.* **832** (2), L20.
- WILLIAMSON, J. 1980 Low-storage Runge-Kutta schemes. *J. Comp. Phys.* **35** (1), 48 – 56.
- WOODHAM, L. D., WICKS, R. T., VERSCHAREN, D. & OWEN, C. J. 2018 The role of proton cyclotron resonance as a dissipation mechanism in solar wind turbulence: A statistical study at ion-kinetic scales. *Astrophys. J.* **856** (1), 49.

- ZHAO, G. Q., LIN, Y., WANG, X. Y., WU, D. J., FENG, H. Q., LIU, Q., ZHAO, A. & LI, H. B. 2020 Observational evidence for solar wind proton heating by ion-scale turbulence. *Geophysical Research Letters* **47** (18), e89720.
- ZOCCO, A. & SCHEKOCHIHIN, A. A. 2011 Reduced fluid-kinetic equations for low-frequency dynamics, magnetic reconnection, and electron heating in low-beta plasmas. *Phys. Plasmas* **18** (10), 102309.